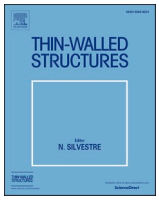
Thin–Walled Structures 224 (2026) 114584



Contents lists available at ScienceDirect

Thin-Walled Structures

journal homepage: www.elsevier.com/locate/tws



Full length article



Residual stress distributions in wire-arc directed energy deposited steel tubular parts

Athina Spinasa [a], Xin Meng [a,b,*], Ben Weber [a], Leroy Gardner [a]

[a] Department of Civil and Environmental Engineering, Imperial College London, London, UK
[b] Department of Civil and Environmental Engineering, National University of Singapore, Singapore

ARTICLE INFO

Keywords:
Digital image correlation (DIC)
Residual stresses
Sectioning method
Tests
Wire arc additive manufacturing (WAAM)
Wire-arc directed energy deposition (DED-Arc)

ABSTRACT

Wire-arc directed energy deposition (DED-Arc), is a metal 3D printing technology that enables the production of large, intricate steel components with significant potential in structural engineering. The cyclic thermal history inherent to the DED-Arc process induces residual stresses, which can influence the structural performance of fabricated components. This study experimentally investigates residual stress distributions in seven DED-Arc steel tubular specimens fabricated using ER90S-D2 welding wire. These include three square hollow section (SHS) tubes with nominal thicknesses of 3.5 mm, 4.5 mm, and 5.5 mm, two 3.5 mm-thick circular hollow section (CHS) tubes with interpass temperatures of 150 °C and 350 °C and two 8 mm-thick oval sections with active and passive cooling. The sectioning method was used to measure residual stresses in both longitudinal and transverse directions. Released strains were recorded using a Demec gauge and, as an alternative, using digital image correlation (DIC); the results showed generally good agreement, but the accuracy of the DIC results was compromised in the case of large out-of-plane deformations. For the SHS tubes, tensile stresses appeared in the corners and compressive stresses in the middle of the faces in the longitudinal direction, while the transverse direction showed peak tensile stresses at the top and bottom. Similar distributions were observed across the SHS thicknesses, except in the thinnest tube, where local buckling altered the pattern. The CHS tubes exhibited high through-thickness bending stresses linked to interpass temperature, while membrane stresses were negligible. In the oval tubes, active cooling led to slightly higher residual membrane stresses. The presented results and findings offer key insights into the residual stress distributions in DED-Arc tubular parts, serving as a sound basis for model validation and the evaluation of structural performance.

1. Introduction

Wire-arc directed energy deposition (DED-Arc), also commonly known as wire arc additive manufacturing (WAAM), is an advanced metal additive manufacturing method integrating arc welding with robotic technology to produce metallic components layer by layer. This technique has gained substantial research and industrial interest due to its efficiency and cost-effectiveness in producing large, intricate metallic parts, particularly suitable for applications in the construction, aerospace, automative and other industries [1–5]. Researchers have increasingly explored the potential of DED-Arc to produce a wide range of steel structural elements, examining their mechanical performance under various loading conditions. Tensile coupon testing has been employed to examine the stress-strain characteristics, while structural tests have explored the load-carrying performance [6–10]. The fatigue life and crack growth behaviour of DED-Arc steel has also been assessed [11–13]. In addition, investigations into steel joints and connections manufactured via DED-Arc have provided insights into their structural behaviour [14,15]. Complementary research has also addressed the integration of computer-aided design and experimental validation for the development of optimised DED-Arc-fabricated steel structures [16,17]. Residual stresses are present in conventional structural steel elements, due to e.g. uneven cooling in hot-rolled sections [18,19], and coiling, uncoiling, forming and welding in cold-formed sections [18,20,21]. The high heat input and repetitive thermal cycles during the DED-Arc process create significant temperature gradients, leading to non-uniform thermal expansion and contraction, which in turn induces residual stresses. Residual stresses can cause issues such as distortion, cracking and reduced buckling resistance and fatigue life in structural components [22–25].

* Corresponding author.
E-mail address: xin.meng@nus.edu.sg (X. Meng).

https://doi.org/10.1016/j.tws.2026.114584
Received 17 September 2025; Received in revised form 22 December 2025; Accepted 25 January 2026
Available online 27 January 2026
0263-8231/© 2026 The Author(s). Published by Elsevier Ltd. This is an open access article under the CC BY license (http://creativecommons.org/licenses/by/4.0/).



Fig. 1. Typical DED-Arc residual stress specimens: (a) SHS, (b) CHS and (c) oval.

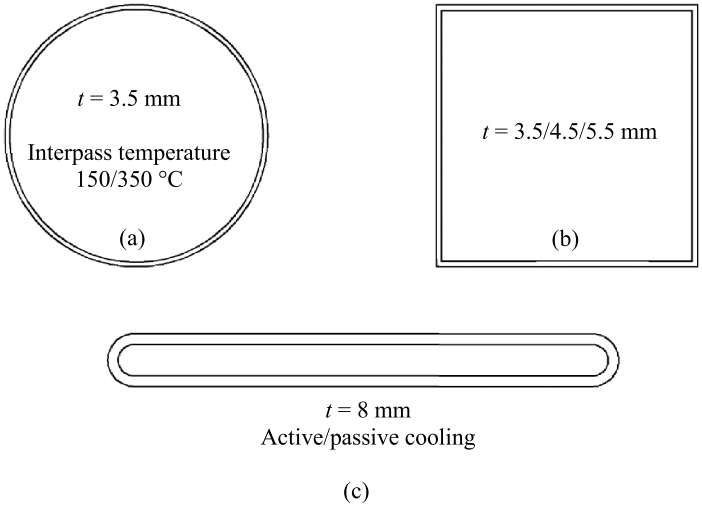


Fig. 2. Schematic diagram of (a) CHS, (b) SHS and (c) oval specimens.

Table 1
Mechanical properties of as-welded ER90S-D2 wire from the wire certificate.

Mechanical property	Nominal	Measured value
Yield strength f_y (MPa)	560	607
Ultimate strength f_u (MPa)	620	637
Elongation at fracture ε_f (%)	18	18
Charpy V-notch impact energy at -70 °C A_v (J)	47	60

The pattern and magnitude of residual stresses in DED-Arc parts have been found to be linked to various factors, such as the heat input, interlayer temperature and part geometry [23,26,27]. Common experimental techniques used for residual stress measurements fall into two main categories: destructive and non-destructive [28]. Destructive methods include hole-drilling, sectioning and contour methods. More specifically, the hole-drilling method is used to measure the near-surface residual stresses by analysing deformations caused by drilling a small hole [29–31]. The sectioning method measures residual stresses released by cutting the specimen into strips [32,33] and the contour method involves cutting the specimen into two pieces and measuring the deformation on the contour surface to determine the residual stresses perpendicular to the contour surface [26,27,34–37]. Non-destructive methods include X-ray diffraction (XRD) and neutron diffraction, which are less commonly used for large-scale parts [22,23,38–40].

Several studies have been conducted recently to explore the residual stress distribution in DED-Arc parts of various materials, including titanium [26,37,39,41], aluminium [23,42], stainless steel [27], carbon steel [22,34] and high-strength steel [22,36,38]. The presence of substrates has been shown to have an impact on the residual stresses in DED-Arc parts [36,38,42,43]. Recent work has also been devoted to the control and reduction of residual stresses, for instance, by preheating the substrate [44–47], in-situ heat treatment [26,31,47] and post-process rolling [37,38]. Additionally, numerical simulations have been increasingly employed to predict residual stress distributions, allowing for their consideration during the DED-Arc design process to mitigate stress-related challenges [48–52].

The majority of existing studies into residual stresses in DED-Arc parts have been focussed on relatively small size specimens and simple geometries (single walls or blocks). The present study aims to understand the magnitudes and patterns of residual stresses in larger-scale DED-Arc steel tubular parts, representative of a common form of element used in structural engineering applications [53–55]. DED-Arc

Table 2
Chemical composition of ER90S-D2 wire in (%) from the wire certificate.

C	Si	Mn	S	Cu	Cr	Mo	Ni	Co	Fe
0.10	0.71	1.89	0.011	0.025	0.04	0.44	0.05	0.013	Balance

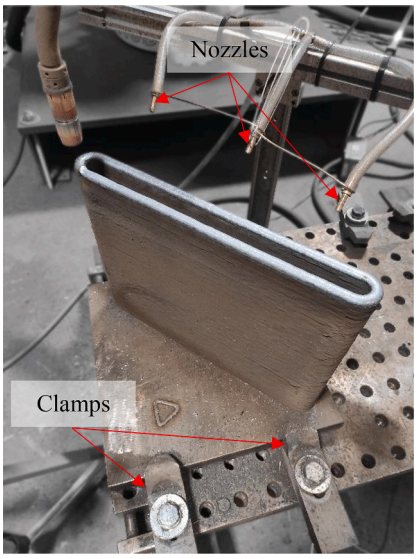


Fig. 3. Application of active cooling for the oval specimen [56].

specimens were printed using ER90S-D2 welding wire and different process parameters. A total of three square hollow section (SHS), two circular hollow section (CHS) and two oval hollow section specimens, produced using different process parameters and cooling methods, were examined. The sectioning method was used for measuring the residual stresses; for the SHS and CHS parts, in addition to a Demec gauge, digital image correlation (DIC) was also employed to measure the released strains. The membrane and bending residual stress distributions were measured in both the longitudinal and the transverse directions for the SHS and oval parts, while for the CHS parts, residual stresses were only measured in the longitudinal direction. The influence of the key process parameters on the residual stress distribution is discussed.

2. Design and manufacture of test specimens

To examine the residual stress distributions in DED-Arc steel tubular parts, seven specimens with three different cross-sectional shapes, including three SHS tubes, two CHS tubes and two ovals, as illustrated in Figs. 1 and 2, were produced by the Dutch manufacturer MX3D using a 6-axis ABB robot equipped with a metal inert gas (MIG) welding system. The oval sections were selected because they are commonly employed for extracting tensile coupons when studying the mechanical properties of DED-Arc steel, while the CHS and SHS specimens were chosen because of their widespread use as structural elements, including in optimised systems. Furthermore, closed DED-Arc profiles are generally more favourable in terms of printing quality relative to open sections. Carbon steel welding wire of grade ER90S-D2 [56] with a 1.2 mm diameter was used as the feedstock material. The as-welded mechanical properties and the chemical composition of the feedstock wire provided in the wire certificate from the manufacturer are reported in Tables 1 and 2, respectively.

The SHS specimens had three different thicknesses – $t = 3.5$ mm, 4.5 mm and 5.5 mm, while an interpass temperature of 350 °C was used for all SHS specimens. For the CHS specimens, the wall thicknesses t were equal to 3.5 mm, while two different interpass temperatures – 150 °C and 350 °C, were employed. The higher interpass temperature of 350 °C was selected as it can reduce the dwell time and enhance productivity. The oval shaped specimens were 8 mm-thick with an interpass temperature of 350 °C. Active cooling was applied to one oval specimen using compressed air from additional nozzles placed in an array along

Table 3
Process parameters used for printing the DED-Arc SHS tubes.

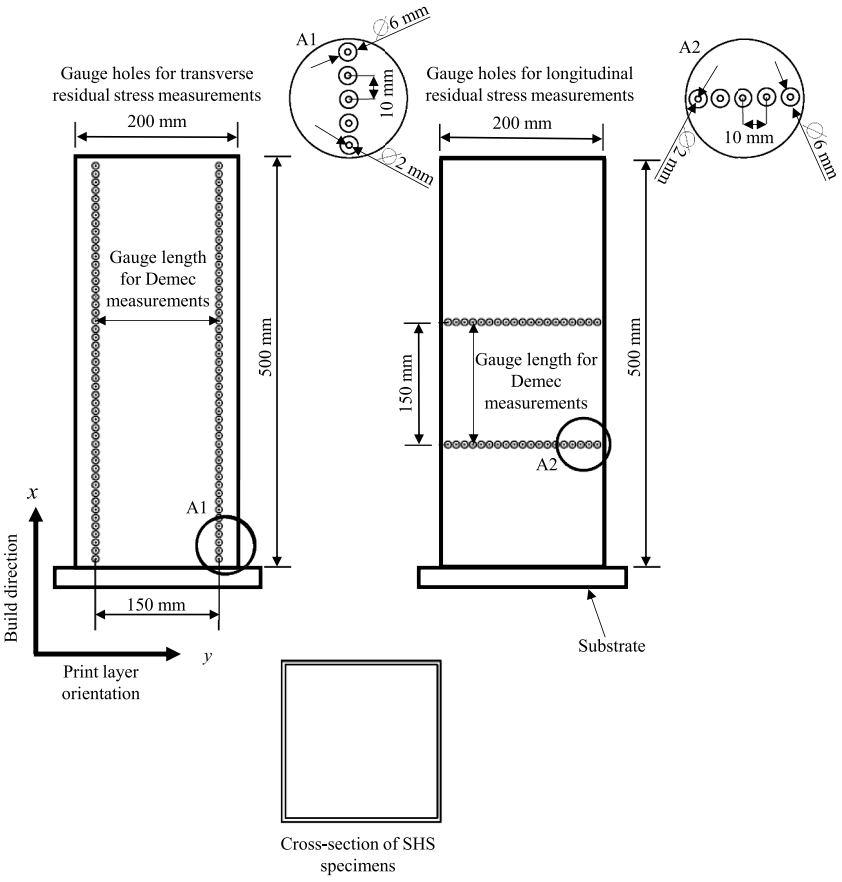
	$t_{nom} = 3.5$ mm	$t_{nom} = 4.5$ mm	$t_{nom} = 5.5$ mm
Wire grade	ER90S-D2	ER90S-D2	ER90S-D2
Wire diameter (mm)	1.2	1.2	1.2
Wire feed rate (m/min)	2.3	2.7	2.3
Travel speed (mm/s)	12	10	9.5
Average layer height (mm)	1.224	1.140	1.315
Interpass temperature (°C)	350	350	350
Stick out (mm)	9–12	9–12	9–12
Welding voltage (V)	14.6	15.6	16.8
Welding current (A)	102	117	142
Shield gas composition	98% Ar, 2% CO_2	98% Ar, 2% CO_2	98% Ar, 2% CO_2
Shield gas flow rate (L/min)	16.0	16.0	16.0
Cooling method	Passive	Passive	Passive
Toolpath	Single pass	Single pass	Single pass

Table 4
Process parameters used for printing the DED-Arc CHS tubes.

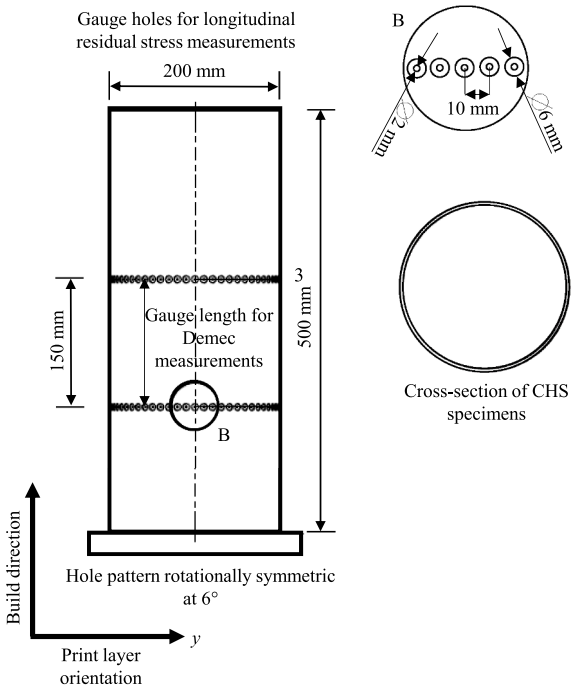
	Low interpass temperature (150 °C)	High interpass temperature (350 °C)
Wire grade	ER90S-D2	ER90S-D2
Wire diameter (mm)	1.2	1.2
Wire feed rate (m/min)	2.3	2.3
Travel speed (mm/s)	12	12
Average layer height (mm)	1.099	1.224
Interpass temperature (°C)	150	350
Stick out (mm)	9–12	9–12
Welding voltage (V)	14.6	14.6
Welding current (A)	102	102
Shield gas composition	98% Ar, 2% CO_2	98% Ar, 2% CO_2
Shield gas flow rate (L/min)	16.0	16.0
Cooling method	Passive	Passive
Toolpath	Single pass	Single pass

Table 5
Process parameters used for printing the DED-Arc ovals.

	Passive cooling	Active cooling
Wire grade	ER90S-D2	ER90S-D2
Wire diameter (mm)	1.2	1.2
Wire feed rate (m/min)	3.5	3.5
Travel speed (mm/s)	9.5	9.5
Average layer height (mm)	1.680	1.680
Interpass temperature (°C)	350	350
Stick out (mm)	9–12	9–12
Welding voltage (V)	16.8	16.8
Welding current (A)	152	152
Shield gas composition	98% Ar, 2% CO_2	98% Ar, 2% CO_2
Shield gas flow rate (L/min)	16.0	16.0
Cooling method	Passive	Active
Toolpath	Double pass	Double pass

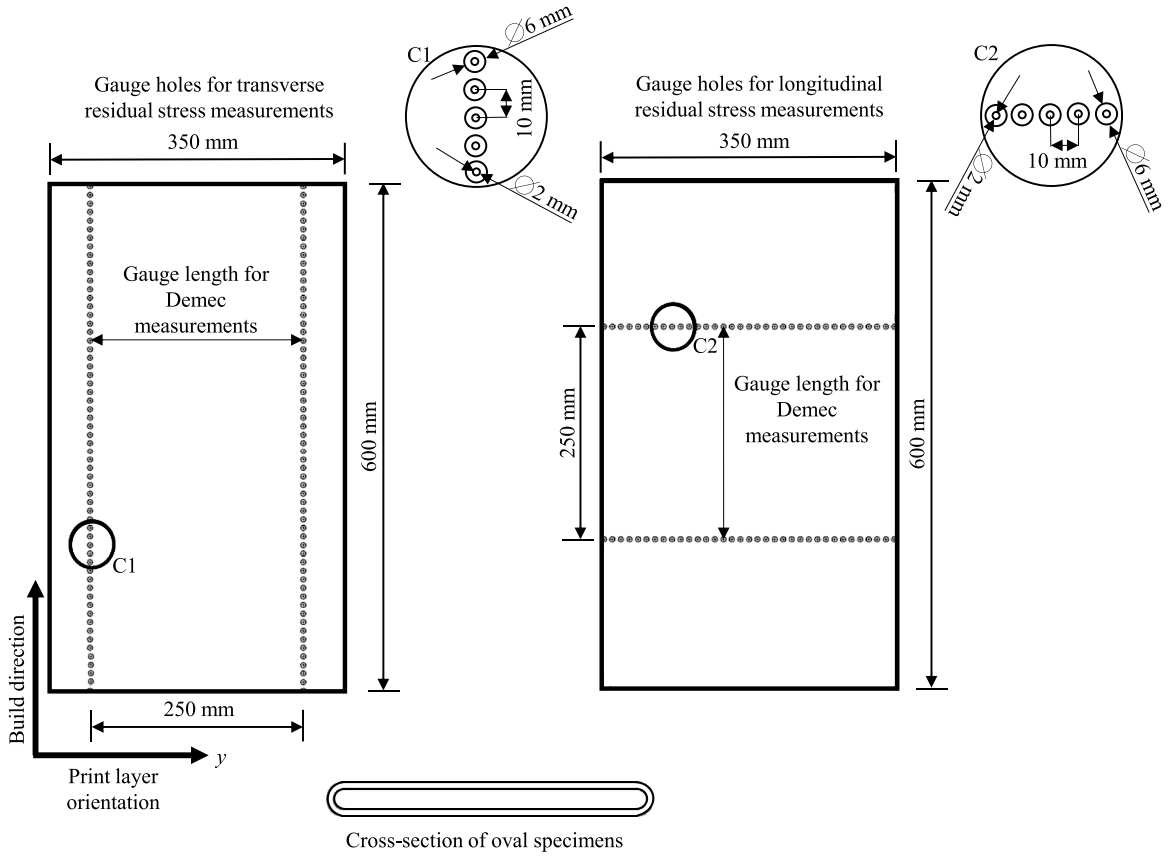


(a)



(b)

Fig. 4. Arrangements of Demec gauge holes on DED-Arc specimens (a) SHS, (b) CHS and (c) ovals.



(c)

Fig. 4. (*continued*).

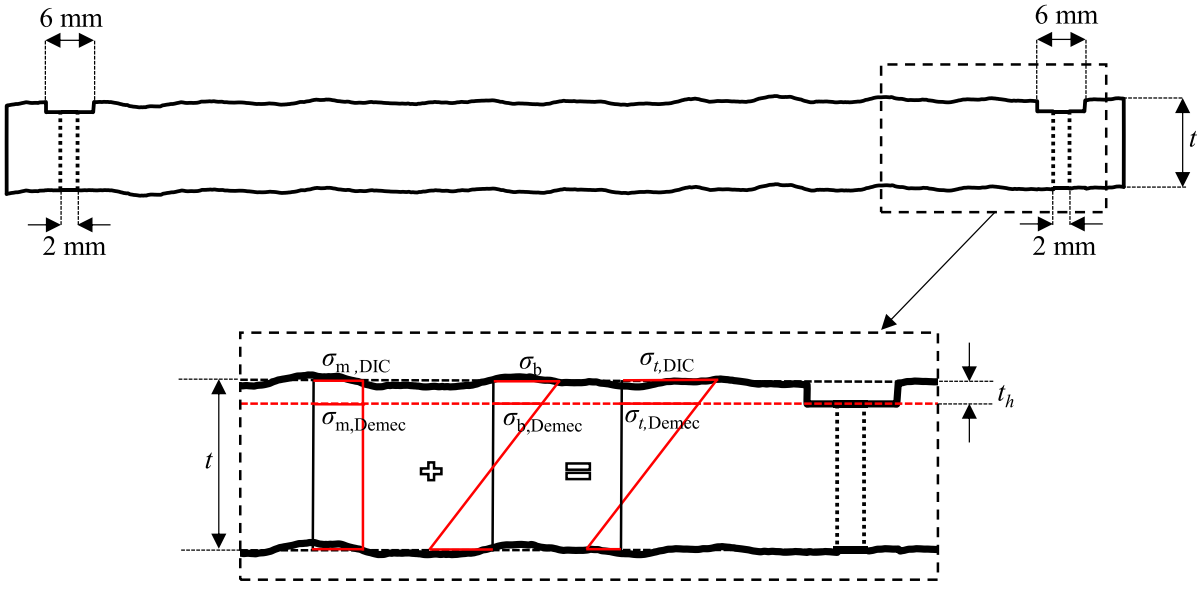


Fig. 5. Graphical illustration of the 6 mm flattened surfaces around the 2 mm Demec holes.

one side of the ovals after the completion of each layer and before the deposition of the next one, as illustrated in Fig. 3. The SHS and CHS specimens were printed on a steel substrate measuring 250 mm × 250 mm × 25 mm, while the ovals were printed on 350 mm × 350 mm × 30 mm S355 steel plates, which were clamped to a steel platform throughout the printing process without preheating being applied prior to deposition, as shown in Fig. 3. The key process parameters used for the SHS, CHS and oval specimens are presented in Tables 3–5, respectively.



Fig. 6. Residual stress measurement steps for (a) SHS, (b) CHS, and (c) oval specimens.



(a) (b) (c)

Fig. 7. (a) Bandsaw removal of the substrate from a CHS specimen, (b) extraction of the four plates from SHS tubes and (c) release of the strips in CHS tubes.

3. Residual stress measurement procedure

The sectioning method, a common destructive technique used for measuring residual stresses in structural steel members [18,32], was employed to measure the residual stresses in the DED-Arc test specimens. For the ovals and SHS specimens, residual stresses in both the longitudinal direction, i.e. along the length of the specimens (x-axis), and the transverse direction, i.e. across the width of the specimens (y-axis), were measured; for the CHS, only the longitudinal residual stresses were examined. Longitudinal residual stresses were measured at the top and middle sections of the SHS and CHS specimens, as space constraints prevented measurements at the bottom. For the oval specimens, residual stresses were recorded at the top, middle and bottom sections. The results revealed a consistent stress distribution along the specimen height, with notably lower magnitudes near the top edge. Therefore, only the measurement procedure and results for the middle sections, where the residual stresses are least influenced by boundary effects, will be presented and discussed. The geometry of each specimen type, together with the arrangements of the holes for Demec gauge measurements at the middle of the tubes and ovals, are presented in Fig. 4. All gauge holes had a diameter of 2 mm and were drilled using a CNC milling machine at a distance of 10 mm between each pair of gauge holes, as shown in Fig. 4. A circular area with a 6 mm diameter around each hole was milled flat to remove surface undulations and facilitate accurate Demec gauge measurements, as illustrated in Fig. 5. The holes were then lightly sanded to eliminate any burrs from the drilling process and cleaned with acetone and air blasting.



Fig. 8. Measuring the gauge length of a strip on a CHS tube using Demec gauge.

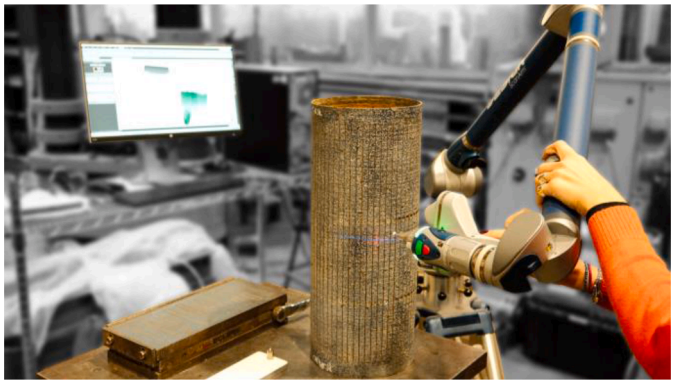


Fig. 9. Laser scanning of a DED-Arc CHS specimen in Step 3.

Residual stresses were released in multiple steps for each type of specimen. For the SHS specimens, the released residual stresses were measured in four steps, as illustrated in Fig. 6(a). In Step 1, the SHS specimen consisted of the SHS tube and the substrate, where the residual stresses after unclamping were preserved. In Step 2, the substrate was removed using a bandsaw, as shown in Fig. 7(a). In Step 3, the four constituent flat plates were extracted using a disk cutter – see Fig. 7(c). Finally, in Step 4, sectioning was performed by means of waterjet cutting, where the residual stresses in the strips were released, while the strips were left attached at one end. For the CHS specimens, as depicted in Fig. 6(b), Steps 1 and 2 were the same as those for the SHS tubes. In Step 3, the CHS specimens were sectioned with two ends remaining intact, and in the last step – Step 4, the longitudinal residual stresses in the strips were released by cutting off the top end using a disk cutter – see Fig. 7(b). For the ovals, the sectioning process was similar to the SHS but without the substrate, as illustrated in Fig. 6(c). It is important to note that the preceding steps did not affect the residual stress distributions due to the negligible heat or plastic deformation induced.

In accordance with the recommendations of the Structural Stability Research Council [57], three repeated readings were taken on each pair of gauge holes using a Demec gauge in each step, as illustrated in Fig. 8. The strip curvature was determined using 3D laser scanning in each step to determine the released bending residual stresses. A FARO Scan Arm, capable of capturing 600,000 points per second with an accuracy of 0.075 mm, was used to obtain the point cloud of the test specimens, as shown in Fig. 9. The scan data processing and determination of the bending residual stresses are described in Section 4.1.

In addition to the Demec gauge measurements, two LaVision StrainMaster compact stereo digital image correlation (DIC) systems were employed to measure the surface strains on the SHS and CHS specimens in all the steps. The specimens were wire brushed and then coated with a random white speckle pattern on a matte black background to provide trackable features for DIC. Fig. 10(a) and 10(b) show the DIC setups for the SHS and CHS specimens, respectively, which remained immovable throughout the measurement process. For the SHS specimens, two DIC systems were utilised to monitor the transverse and longitudinal stresses separately. The specimens were placed on a

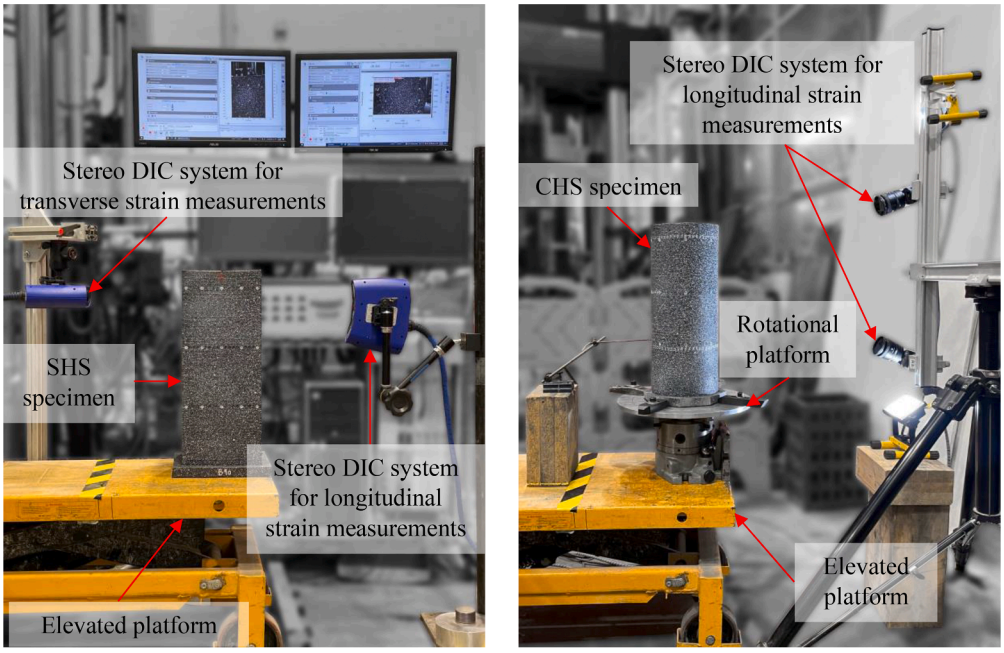


Fig. 10. DIC setup for (a) SHS and (b) CHS specimens.

platform to record the strains in the strips at each step. The same setup principle was used for the CHS specimens but using one DIC system, along with a rotational platform to capture the entire circumference of the tubes. For each step, five DIC images were acquired. The measured surface strains released from sectioning, processed using DaVis 10 [58], were utilised as an alternative approach to determining the residual stresses, as discussed in Section 5.2.4.

4. Determination of membrane and bending residual stresses

In this section, the procedure for determining the membrane and bending residual stresses from the measurements are described.

4.1. Bending stresses

The laser scan data were utilised to determine the bending residual stresses. For each specimen, the scan data from all the measurement steps were initially cleaned and re-orientated using Geomagic Wrap [59]. The convolution method was then employed to determine the coordinates of the holes along with the z coordinate of all the points of the created point cloud, as shown in Fig. 11, where the z coordinates of all data points along the line formed between the two holes in the xy plane are illustrated, showing their deformation in the xz plane for two consecutive steps. The difference in the z coordinate between two steps Δz was used to calculate the change in curvature of the strip. The locations of the holes served as a reference to account for any elongation or shrinkage Δl of the strip due to the residual stresses, as illustrated in Fig. 11. Finally, the bending residual stresses σ_b were determined by assuming a linearly varying through-thickness stress pattern, as given by Eq. (1):

$$\sigma_b = E\,\frac{z}{\Delta R} \tag{1}$$

where E is the Young's modulus taken equal to the average measured value from the as-built coupon tests reported in [60], z is the distance between the surface and the neutral axis of the strips (assumed to be $t/2$, where t is the average strip thickness determined based on the scan data), and ΔR is the average change in curvature based on the computed Δz values of the points along the length of each strip, assuming that the curvature was constant along the length of the strips.

4.2. Membrane residual stresses

Membrane residual stresses were calculated using both the Demec gauge and the DIC data for comparison. The Demec gauge measurements, which were taken along the chord rather than the arc [57] – see Fig. 12, were initially corrected to remove the effects of strip curvature. The strip curvature was assumed to be constant, while the Demec gauge length was taken to be the chord length L_{chord}, as shown in Fig. 12. The relationship between the angle of curvature θ and the chord length L_{chord}, is given by Eq. (2):

$$\sin(\theta/2) = \frac{L_{chord}}{2R} \tag{2}$$

where R is the radius of the curvature of the strip obtained using the laser scan data. Three corrections are required to convert the Demec gauge measurements to membrane residual stresses. First, the conical points of the Demec gauge, positioned inside the gauge holes on the strip, resulted in an offset Δ from the conical point to the gauge hole centreline, as shown in Fig. 13. Assuming complete contact of the conical point with the gauge hole circumference and constant strip curvature, the offset Δ can be determined using Eq. (3):

$$\Delta = \frac{d_h}{2}\tan\varphi \times \sin\left(\frac{\theta}{2}\right) \tag{3}$$

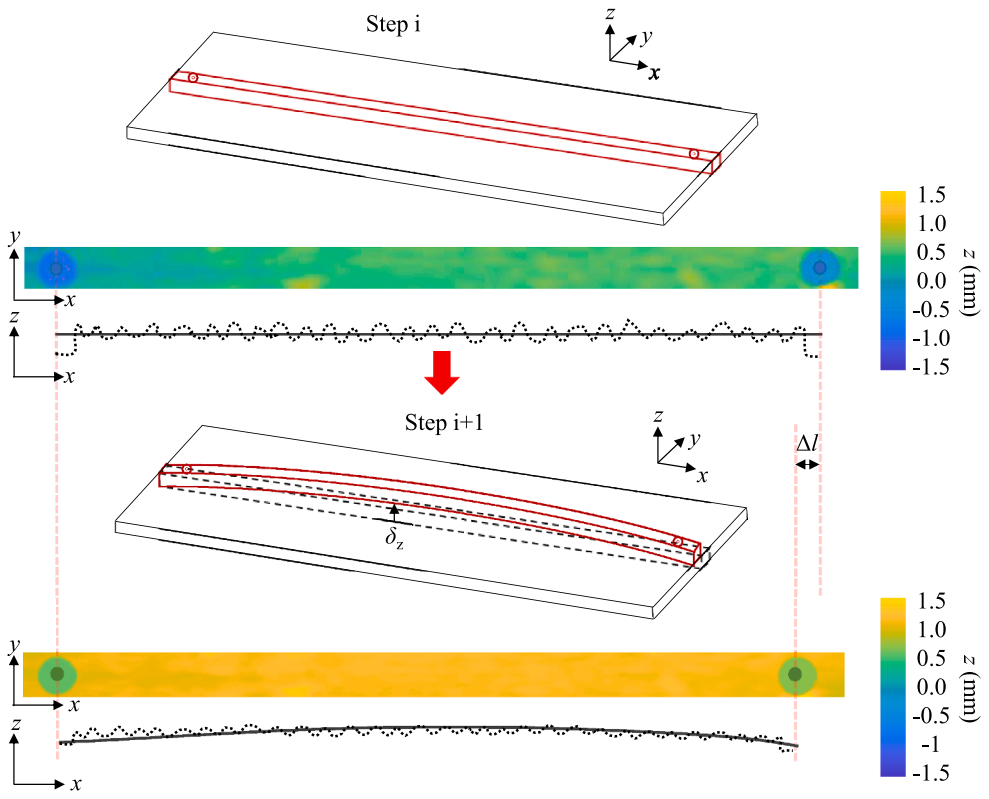


Fig. 11. Plan views (*xy* plane) and side profiles (*xz* plane) of the data points of a strip in two subsequent steps.

where d_h is the gauge hole diameter, θ is the curvature angle and φ is half the internal angle of the conical point – see Fig. 13. The corrected chord length $L_{chord,c}$ considering the offset Δ and a revised angle of curvature θ_c from Eq. (2), was converted to the arc length L_{arc} at the height of the surface of the gauge holes (illustrated in Fig. 14) using Eq. (4).

$$L_{arc} = R\theta_c \tag{4}$$

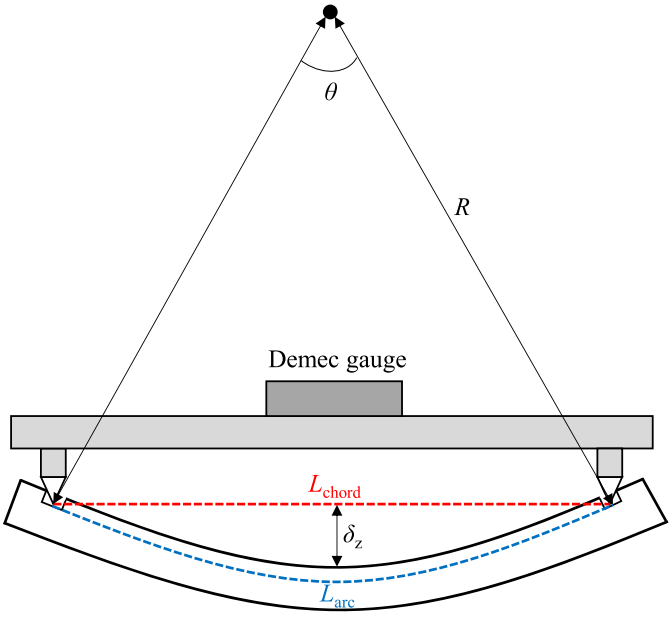


Fig. 12. Demec measurements along chord length and definition of angle of curvature θ.

Assuming an elastic material response, the residual stresses between two steps measured by the Demec gauge $\sigma_{t,Demec}$ can be calculated using Eq. (5), where $L_{arc,i}$ and $L_{arc,i+1}$ are the arc lengths for two steps and E is the Young's modulus. Note that $\sigma_{t,Demec}$ is the total residual stress at the height of the machined hole surface, as illustrated in Fig. 5. The membrane residual stresses based on the Demec measurements $\sigma_{m,Demec}$ can be calculated using Eq. (6), where t_h is the depth of the machined hole surface, as illustrated in Fig. 5.

$$\sigma_{t,Demec} = \frac{L_{arc,i} - L_{arc,i+1}}{L_{arc,i}} E \tag{5}$$

$$\sigma_{m,Demec} = \sigma_{t,Demec} - \sigma_{b,Demec} = \sigma_{t,Demec} - \sigma_b \frac{t/2 - t_h}{t/2} \tag{6}$$

Alternatively, based on the DIC data, the total averaged surface stresses $\sigma_{t,DIC}$ for each strip at all the steps can be determined. Assuming an elastic material response, the membrane residual stresses based on the DIC measurements $\sigma_{m,DIC}$ can be calculated using Eq. (7).

$$\sigma_{m,DIC} = \sigma_{t,DIC} - \sigma_b \tag{7}$$

5. Results and discussion

The residual stresses measured in all seven DED-Arc steel tubular parts, including both the membrane and bending components in the longitudinal and transverse directions, are presented in this section. For the membrane components, negative values correspond to residual compression, while positive values indicate tensile residual stresses. For the bending components, positive values indicate tensile residual stresses on the outer surface, while negative values show the presence of tensile residual stresses on the inner surface. Note that the longitudinal and transversal residual stress distributions were found to be approximately in self-equilibrium in each different specimen and step, supporting the suitability and accuracy of the measurement process.

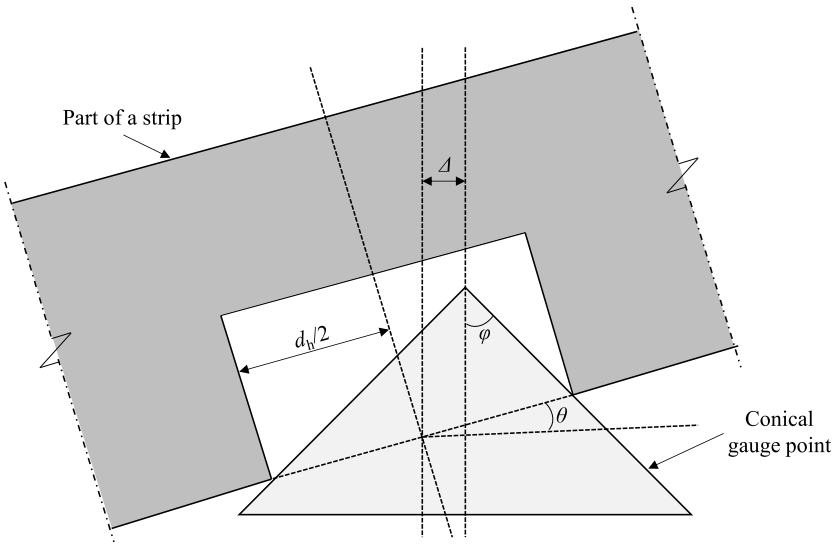


Fig. 13. Gauge hole correction.

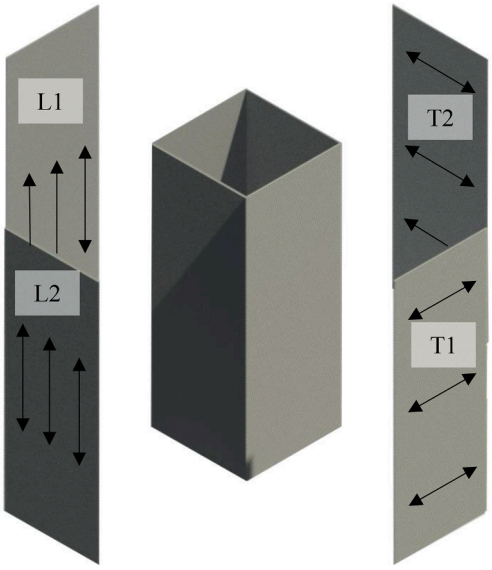


Fig. 14. Orientation of residual stress strips on the four faces of the SHS tubes.

5.1. Results

5.1.1. SHS specimens

The membrane and bending residual stresses of the three SHS tubes are presented in Fig. 15 for the transverse direction and in Fig. 16 for the longitudinal direction. The residual stress distributions in the DED-Arc parts both with and without substrates are shown. T1 and T2 are the faces used for the transverse residual stress measurements and L1 and L2 indicate the faces used for measuring the longitudinal residual stresses – see Fig. 14. Tables 6 presents the maximum $\sigma_{m,Demec,max}$ (tension) and minimum $\sigma_{m,Demec,min}$ (compression) membrane residual stress and the ratios $\sigma_{m,Demec,max}/f_y$ and $\sigma_{m,Demec,min}/f_y$ of the SHS tubes, where f_y is the yield strength of the tubes. The yield strength f_y was estimated by interpolation using the average thickness of the examined part based on the average machined material test results reported in [60], as illustrated in Fig. 17. Note that for each result presented in Table 6, the first value is the residual stress in the specimen after the substrate removal, while the second value in brackets is that in the specimen with the substrate attached.

5.1.2. CHS specimens

The membrane and bending residual stresses in the two CHS tubes in the longitudinal direction around the circumference both before and after the substrate removal are depicted in Fig. 18.

5.1.3. Oval specimens

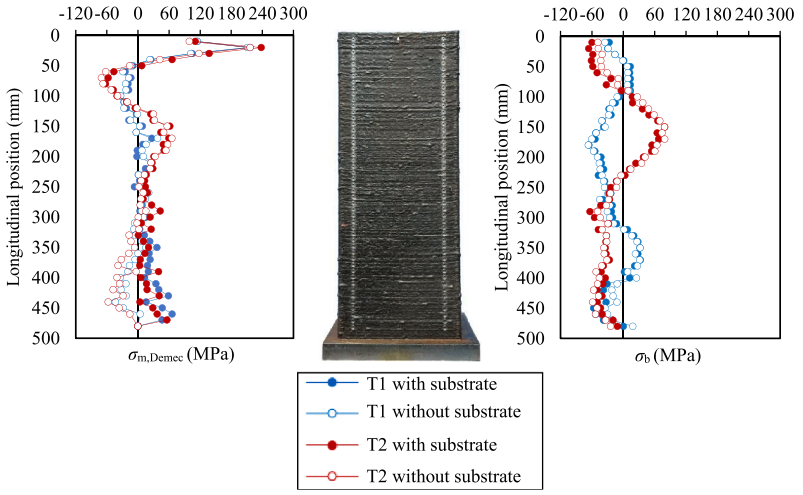
The membrane and bending residual stresses in the two oval specimens without the substrate in the transverse and longitudinal directions are illustrated in Figs. 19 and 20, respectively. Table 7 presents the maximum $\sigma_{m,Demec,max}$ (tension) and minimum $\sigma_{m,Demec,min}$ (compression) membrane residual stress and the ratios $\sigma_{m,Demec,max}/f_y$ and $\sigma_{m,Demec,min}/f_y$ in the oval tubes.

5.2. Discussion of the results

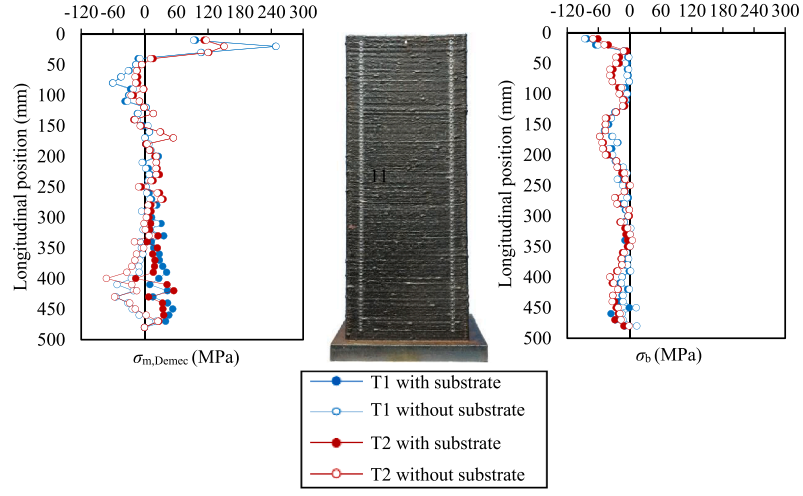
During the manufacturing process of DED-Arc tubular members, residual stresses develop in both the longitudinal and transverse directions as the material undergoes non-uniform heating and cooling. In this section, the residual stresses observed at various measurement stages are analysed. Additionally, the results obtained using DIC are compared with those obtained using the Demec method to assess the applicability of DIC to residual stress measurements. Finally, the influence of material thickness, interpass temperature and cooling method on the residual stress distributions in DED-Arc SHS, CHS and oval tubes, is discussed.

5.2.1. SHS specimens

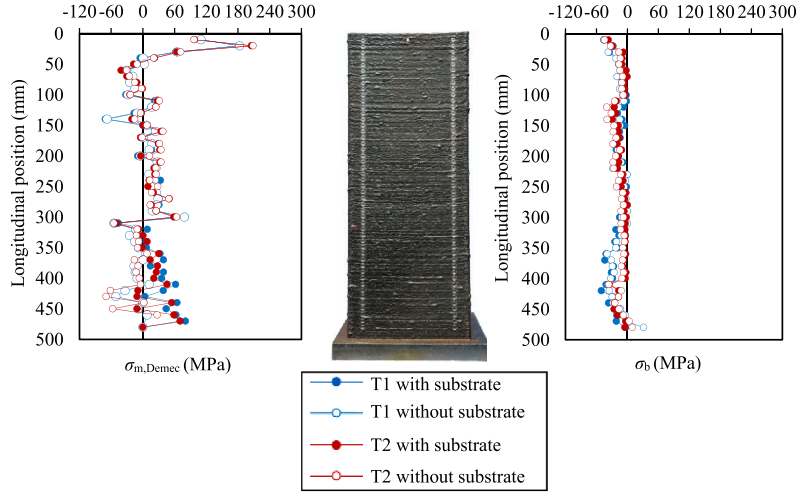
5.2.1.1. Transverse residual stresses. As shown in Fig. 15(a), (c), and (e), and due to the considerable height of the DED-Arc specimens, the residual stresses in the upper half of the tubes presented the maximum tensile membrane stresses. At the top of the SHS tube, higher tensile residual stresses were observed since this region cools last during the deposition process. Towards the middle of the tubes, there was a transition to compressive stresses in order to maintain equilibrium. Finally, the bottom of the tubes showed mainly tensile residual stresses, leading to a final distribution of transverse membrane residual stresses characterised by a tension-compression-tension pattern from top to bottom. Before the substrate removal, the maximum tensile residual stress for all the SHS tubes was around 200 MPa, while the maximum compressive residual stress was around -50 MPa, as summarised in Table 6. Several existing studies have been conducted into the transverse residual stress distribution in relatively short DED-Arc specimens before the substrate



(a) Membrane residual stresses – t_{nom} = 3.5 mm (b) Bending residual stresses – t_{nom} = 3.5 mm



(c) Membrane residual stresses – t_{nom} = 4.5 mm (d) Bending residual stresses – t_{nom} = 4.5 mm



(e) Membrane residual stresses – t_{nom} = 5.5 mm (f) Bending residual stresses – t_{nom} = 5.5 mm

Fig. 15. Distribution of the transverse membrane and bending residual stresses in the SHS specimens.

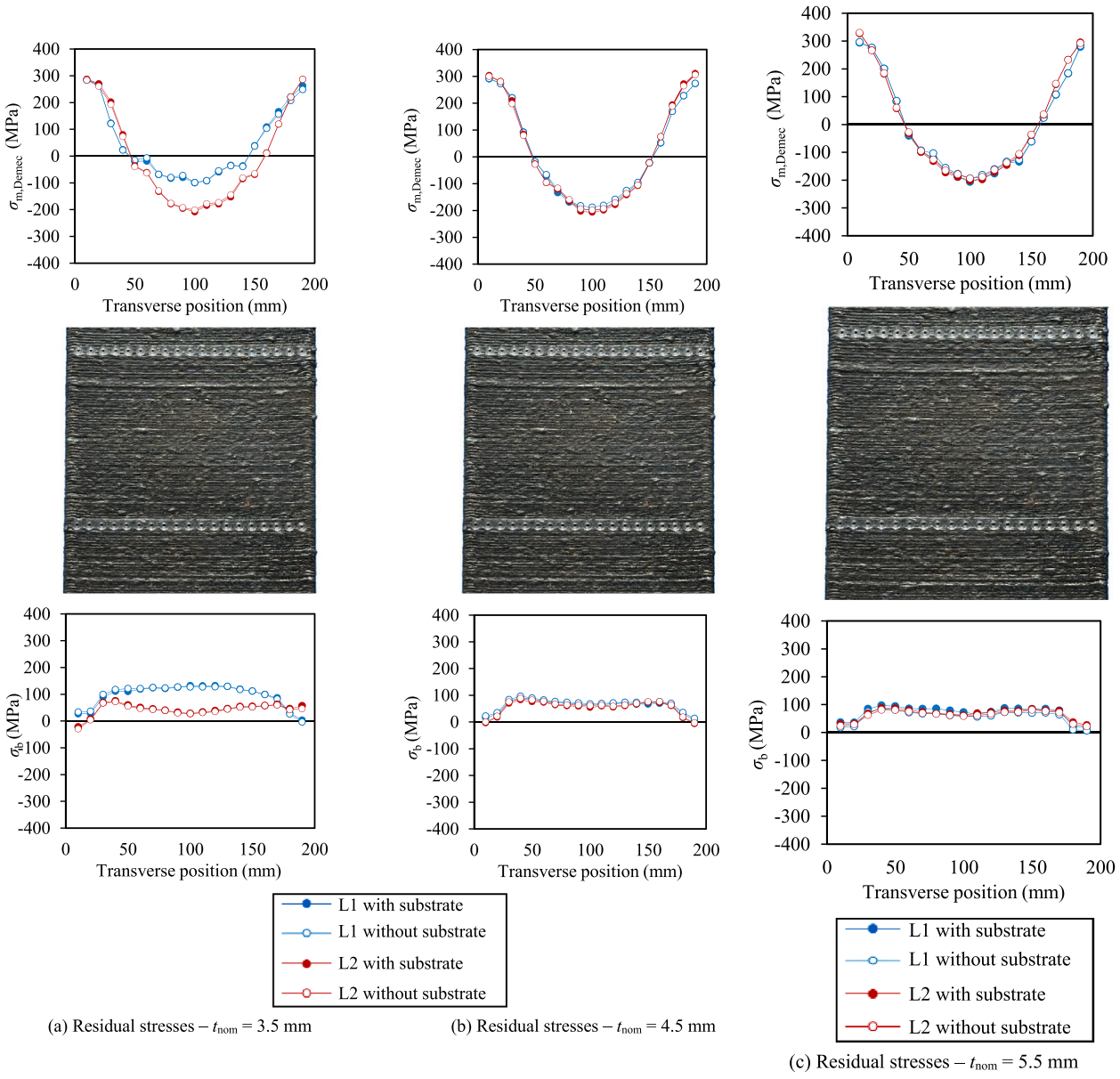


Fig. 16. Distribution of the longitudinal membrane and bending residual stresses in the SHS specimens.

removal [22,34–37,47,50], where removal from the substrate has a more pronounced effect on the overall residual stress distribution, showing that compressive stresses predominantly occur at the top of the DED-Arc specimens, whereas tensile stresses are more pronounced near the bottom. For taller DED-Arc specimens, which are expected to be more common for structural applications, the influence of the substrate on the residual stress distribution in the DED-Arc parts, which is mainly in the region near the substrate and diminishes in higher layers, will be insignificant

Finally, comparing the transverse residual stress profiles before and after removing the substrate, membrane residual stresses changed mainly near the bottom of the tube, as the removal of the substrate released some tensile stresses, occasionally converting the tensile region at the bottom of the tube to compression, which was also reported in Ahmad et al. [26]. Transverse bending residual stresses remained relatively low in magnitude (typically below 60 MPa) and unaffected by the removal of the substrate, as indicated in Fig. 15(b), (d), and (f); an exception was the thinnest specimen due to the influence of elastic

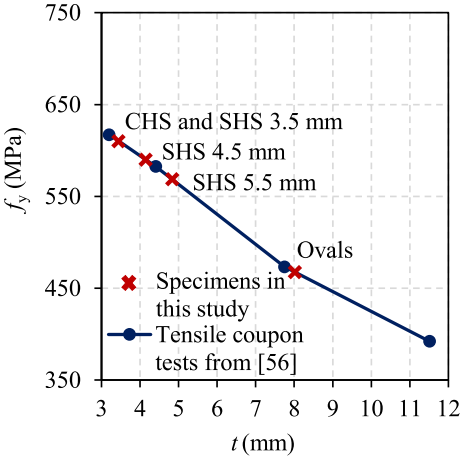
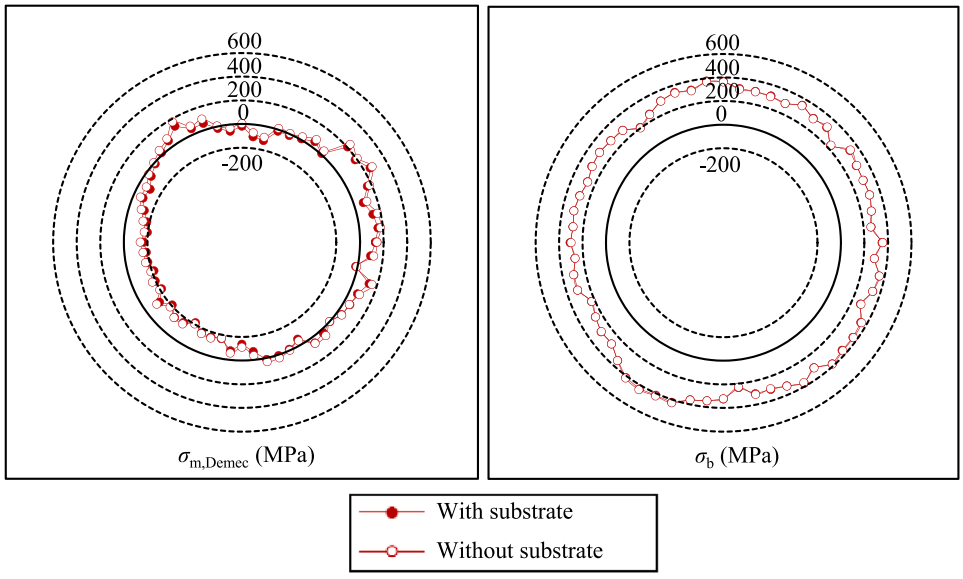


Fig. 17. Yield strength according to the measured thickness of the tubular members.

Table 6
Summary of peak membrane residual stresses in the SHS tubes.

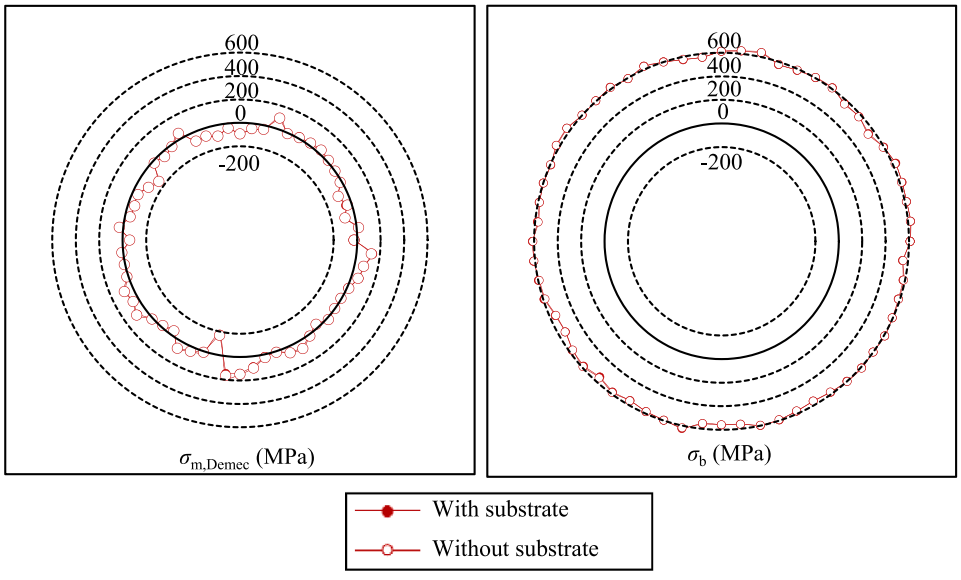
t_{nom} (mm)	Direction	Face	$\sigma_{m,Demec,max}$ (MPa)	$\sigma_{m,Demec,max}/f_y$	$\sigma_{m,Demec,min}$ (MPa)	$\sigma_{m,Demec,min}/f_y$
3.5	Transverse	T1	211 (217)	0.35 (0.36)	-44 (-34)	-0.07 (-0.06)
		T2	217 (238)	0.36 (0.39)	-70 (-62)	-0.12 (-0.10)
	Longitudinal	L1	284 (285)	0.47 (0.47)	-99 (-99)	-0.16 (-0.16)
		L2	287 (288)	0.47 (0.47)	-202 (-208)	-0.33 (-0.34)
4.5	Transverse	T1	249 (248)	0.42 (0.42)	-60 (-61)	-0.10 (-0.10)
		T2	151 (150)	0.26 (0.25)	-72 (-21)	-0.12 (-0.04)
	Longitudinal	L1	292 (291)	0.49 (0.49)	-188 (-199)	-0.32 (-0.34)
		L2	305 (311)	0.52 (0.53)	-199 (-207)	-0.34 (-0.35)
5.5	Transverse	T1	183 (182)	0.32 (0.32)	-68 (-71)	-0.12 (-0.12)
		T2	209 (206)	0.37 (0.36)	-69 (-50)	-0.12 (-0.09)
	Longitudinal	L1	297 (294)	0.52 (0.52)	-195 (-207)	-0.34 (-0.36)
		L2	329 (327)	0.58 (0.57)	-194 (-201)	-0.34 (-0.35)

Note: values in brackets are residual stresses in specimens with substrate attached.



(a) Membrane residual stresses – high interpass temperature

(b) Bending residual stresses – high interpass temperature



(c) Membrane residual stresses – Low interpass temperature

(d) Bending residual stresses – low interpass temperature

Fig. 18. Distribution of the longitudinal membrane and bending residual stresses in the CHS specimens.

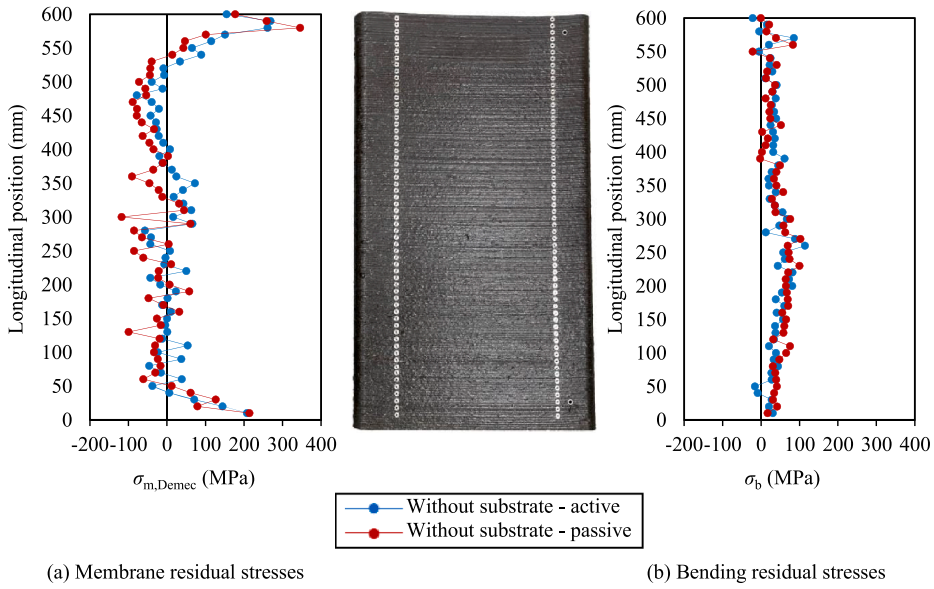


Fig. 19. Distribution of the transverse residual stresses in the oval specimens.

buckling, which is discussed further in Section 5.2.1.3.

5.2.1.2. Longitudinal residual stresses. The longitudinal membrane and bending residual stresses measured in the DED-Arc SHS tubes are shown in Fig. 16. The average maximum tensile residual stress was around 300 MPa near the tube corners, while the maximum compressive residual stress was around -180 MPa, occurring at the middle of the tube face – see Table 6. The tube corners cooled at a slower rate compared to the flat surfaces, which partially accounts for the longitudinal compressive stresses in the flat faces and tensile stresses in the corners [58]. Thermal-mechanical modelling of the printing process is needed to fully explain the observed residual stress distributions. The effect of substrate removal on the longitudinal membrane and bending stresses was insignificant, as the measurements were taken away (approximately 100 mm) from the substrate.

5.2.1.3. Influence of wall thickness. In both the transverse and longitudinal directions, the membrane and bending residual stresses were found to be largely independent of the tube thickness, displaying similar magnitudes and patterns across all SHS specimens, as shown in Fig. 21. The magnitude and pattern of the bending residual stresses for the 4.5 mm and 5.5 mm-thick SHS tubes are also comparable. The 3.5 mm-thick tube exhibited a different residual stress profile between the two repeated faces, as shown in Figs. 15(b) and 16(a). This discrepancy was caused by elastic buckling of the 3.5 mm-thick plated elements under residual compression, altering the residual stress distributions; similar observations were made by Meng et al. [62]. The plate slenderness $c/t\varepsilon$, as specified in EN 1993-1-1:2022 [63], where c is the width of the flat portion of the plate, t is the average thickness of the tube and $\varepsilon = \sqrt{\frac{235}{f_y}}$, was equal to 92 for the 3.5 mm-thick plated parts, which is significantly higher than the Class 3 slenderness limit of 38, indicating high susceptibility to local buckling. The out-of-plane deformations of the four faces of the 3.5 mm specimen, caused by elastic local buckling triggered by the compressive residual stresses, are shown in Fig. 22. The pattern of deformations mirrors the typical elastic buckling mode shape of SHS [64,65]. Overall, although the 3.5 mm, 4.5 mm and 5.5 mm thickness tubes were manufactured with different heat input, this was found to have insignificant influence on the residual stress distribution.

5.2.2. CHS specimens

5.2.2.1. Longitudinal residual stresses. Fig. 18(a) and (c) show that the longitudinal membrane residual stresses in the DED-Arc CHS fluctuated around zero without a distinct pattern, due to the axisymmetry of the specimens. The bending residual stresses, as illustrated in Fig. 18(b) and (d), were shown to be practically uniform around the circumference due again to the axisymmetry, with the outer surface in residual tension, and of significant magnitude. This pattern can be explained by the fact that the outer surface cools more quickly than the inner surface. As the inner surface cools, its contraction is restricted by the outer surface, causing circumferential compressive stress on the outer surface and tensile stress on the inner surface, which, due to the Poisson effect, creates longitudinal tensile stresses on the outer surface and compressive in the inner surface [61]. Additionally, the residual stresses, both membrane and bending, were not affected by the removal of the substrate, again as the measurements were taken away from the substrate.

5.2.2.2. Influence of interpass temperature. The bending residual stresses in the CHS tube with the low interpass temperature (150 °C) were shown to approach the yield strength, around 600 MPa, which is nearly twice as high as those observed in the CHS tube with the high interpass temperature (350 °C). This is likely to be linked to the higher thermal gradients induced during printing for the low interpass temperature. Owing to the highly complex thermal history of DED-Arc parts, thermal-mechanical simulation of the printing process is required to gain a deeper insight into the influence of interpass temperature and toolpath on the resulting residual stresses; this will be conducted in future research, and the test data will provide the experimental basis for model validation.

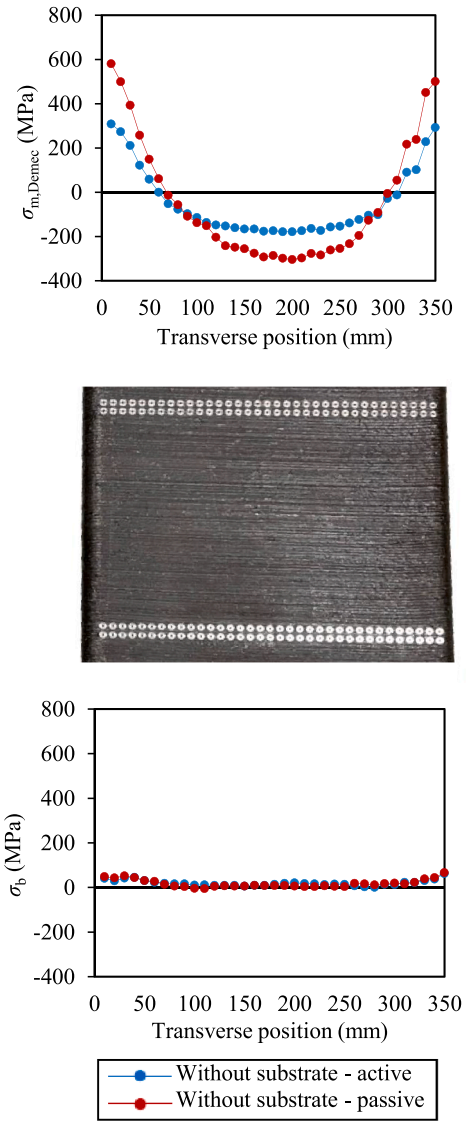


Fig. 20. Distribution of the longitudinal residual stresses in the oval specimens.

5.2.3. Oval specimens

5.2.3.1. Transverse residual stresses. In the transverse direction, as shown in Fig. 19(a), the membrane residual stress pattern in the DED-Arc oval tubes is similar to that in the SHS tubes, with high tension near the top and relatively low magnitudes of residual stress in the remainder of the specimens. In terms of transverse bending residual stresses, as shown in Fig. 19(b), a consistent pattern of tensile bending residual stresses on the outer surface, with an average magnitude of around 100 MPa, was observed.

5.2.3.2. Longitudinal residual stresses. The longitudinal membrane residual stresses in the DED-Arc oval tubes also exhibited similar patterns to the SHS tubes, with tension near the corners and self-equilibrating compression in the middle of the flat faces. This pattern is attributed to the slower cooling in the corner regions [61]. Longitudinal bending residual stresses were shown to be fairly uniform across the width of the ovals with a relatively low magnitude, below 70 MPa, as shown in Fig. 20.

5.2.3.3. Influence of active cooling. In the transverse direction, the distribution of the membrane residual stresses was comparable between the actively and passively cooled ovals, as shown in Table 7. However, the actively cooled oval displayed lower magnitudes of longitudinal membrane residual stress, consistent with the findings of Fan et al. [66]. Thermal-mechanical modelling of the printing process is needed to fully explain the influence of active cooling on the residual stress distribution. Finally, the bending residual stresses in both the transverse and the longitudinal directions were insensitive to the cooling method.

5.2.4. Evaluation of DIC results

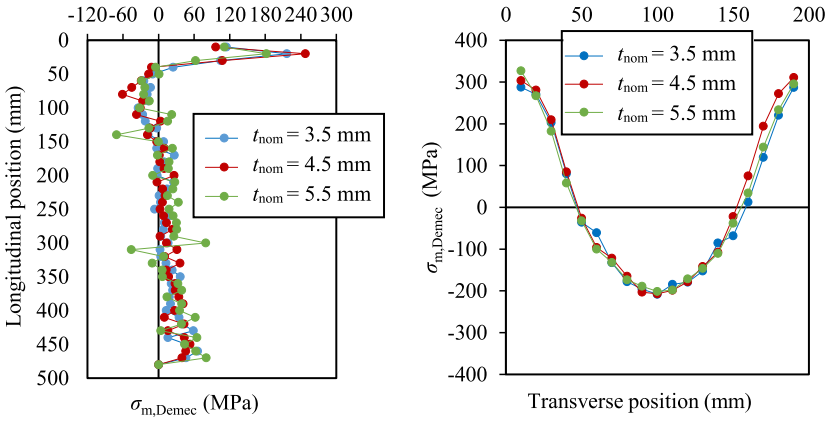
Comparisons between membrane residual stress measurements determined using the Demec gauge and DIC are presented in Fig. 23. Fig. 23(a) compares the longitudinal residual stresses in the L2 face of the 4.5 mm-thick SHS tube, before the substrate removal, measured using the DIC and the Demec technique. The DIC method shows good accuracy in measuring membrane residual stresses, producing results comparable to those based on the Demec technique. However, discrepancies between the two methods can be observed in Fig. 23(b) and (c) for the membrane residual stresses of the L2 face of the 3.5 mm-thick SHS tube and the CHS tube with the low interpass temperature, which are attributed mainly to the increased level of error for DIC when out-of-plane movement is present and specimen positioning and repositioning between successive measurements. This limitation is particularly significant in residual stress measurements where the level of strain to be measured is relatively low (typically around 0.0005). Prior to the experiment, the calibrated DIC system was used to measure an undeformed sample placed at different positions, from which the fictitious strain recorded was considered to be the DIC measurement error. The fictitious strain obtained was around 0.0004, on average, which is relatively high when compared with the strains to be measured associated with residual stresses in this study (around 0.0005). Hence, the DIC measurements were found not to be sufficiently accurate for evaluating residual stresses in the present study. The measurement accuracy can be improved by optimising the DIC setup, such by using as a larger stereo angle and a more controlled environment [67]; this is to be explored in future studies.

6. Conclusions

In the present study, the distribution of residual stresses in wire-arc directed energy deposition (DED-Arc), also commonly known as wire arc additive manufacturing (WAAM), steel tubular members has been examined, and the effects of part geometries, cooling methods and interpass temperatures have been investigated. The sectioning method was employed to investigate seven DED-Arc specimens with square, circular and oval-shaped cross-section profiles. A combination of Demec

Table 7
Summary of peak membrane residual stresses in the ovals.

Cooling method	Direction	$\sigma_{m,Demec,max}$ (MPa)	$\sigma_{m,Demec,max}/f_y$	$\sigma_{m,Demec,min}$ (MPa)	$\sigma_{m,Demec,min}/f_y$
Active	Transverse	278	0.59	-81	-0.17
	Longitudinal	319	0.68	-184	-0.39
Passive	Transverse	353	0.76	-120	-0.26
	Longitudinal	593	1.27	-311	-0.66



(a) Transverse residual stresses (b) Longitudinal residual stresses

Fig. 21. Comparison of typical membrane residual stresses in DED-Arc SHS tubes before the substrate removal.

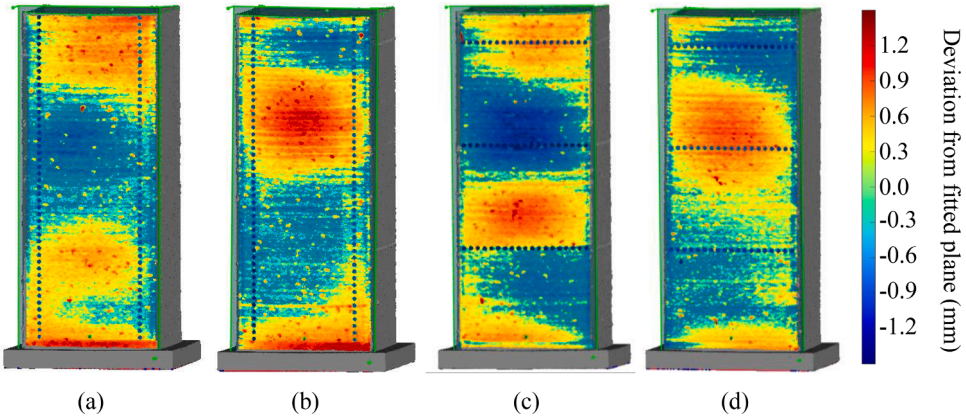


Fig. 22. Deviation maps of the (a) T1 face, (b) T2 face, (c) L1 face and (d) L2 face from fitted planes for the 3.5 mm-thick SHS tube.

gauge, laser scanning and digital image correlation (DIC) was used to measure the strain released from sectioning. Residual stress distributions in both the transverse and longitudinal directions were examined.

The square hollow section (SHS) tubes showed, in the longitudinal direction, tensile residual stresses in the corners and compressive residual stresses in the middle of the flat faces, while in the transverse direction, the lower and upper parts of the tubes exhibited locally high tensile residual stresses. The SHS tubes with different thicknesses exhibited similar residual stress distributions, but the thinnest SHS tube underwent elastic local buckling under the residual compression, which altered the pattern. The circular hollow section (CHS) specimens showed an axisymmetrical residual stress profile around the tube circumference. The longitudinal bending residual stresses were shown to be significant, with residual tension on the outer surface and interpass temperature playing a key role in the bending stress magnitude. For the oval hollow section specimens, the residual stress distribution was similar to the SHS, with active cooling reducing both the tensile and compressive longitudinal residual stresses compared to passive cooling. DIC was shown to be effective for residual stress measurements in some cases, but the accuracy can be negatively affected by the increased measurement error due to out-of-plane movement. Thermal-mechanical simulation of the printing process is needed in future research to gain a deeper insight into the formation of residual stresses in DED-Arc parts, for which the results presented herein will serve as a valuable experimental basis for model validation.

CRediT authorship contribution statement

Athina Spinasa: Writing – original draft, Visualization, Software, Methodology, Investigation, Formal analysis, Data curation. **Xin Meng:** Writing – review & editing, Supervision, Methodology, Investigation, Formal analysis, Conceptualization. **Ben Weber:** Writing – review &

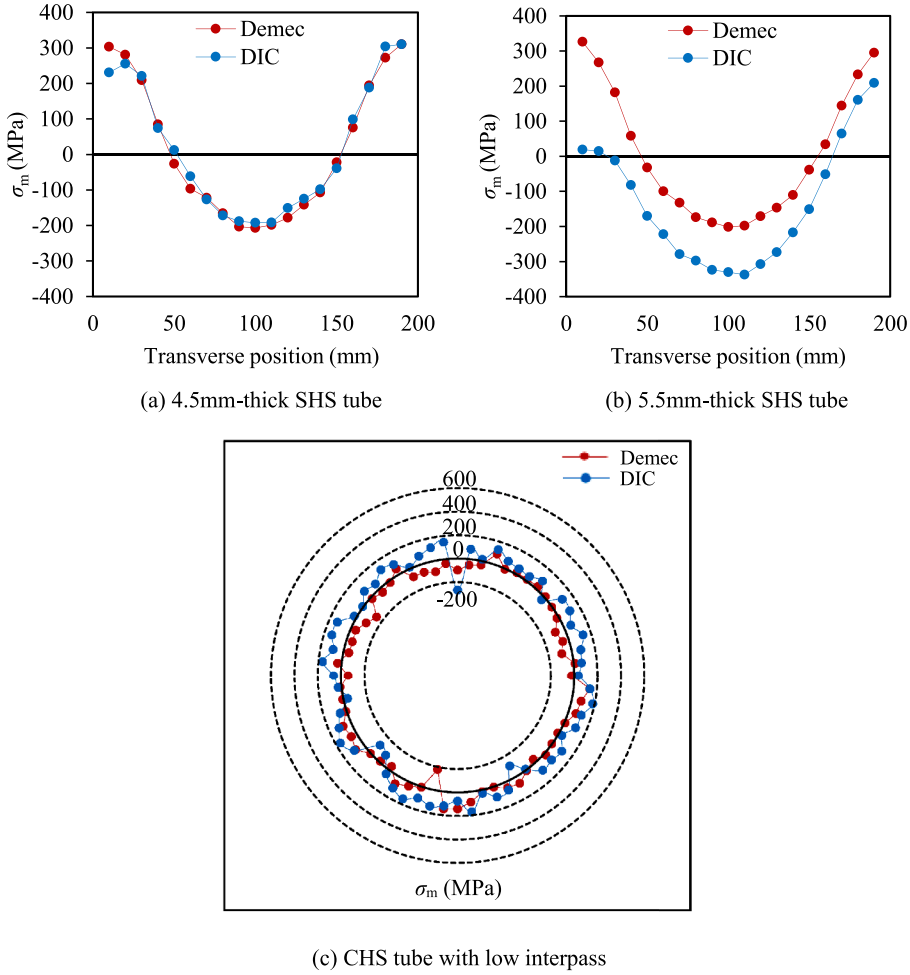


Fig. 23. Comparison of DIC and Demec longitudinal membrane residual stresses before the substrate removal of the (a) T2 face of the 4.5 mm-thick SHS tube, (b) T2 face of the 3.5 mm-thick SHS tube and (c) CHS tube with low interpass temperature.

editing, Methodology, Investigation, Conceptualization. **Leroy Gardner:** Writing – review & editing, Supervision, Resources, Project administration, Funding acquisition, Formal analysis, Conceptualization.

Declaration of competing interest

The authors declare that they have no known competing financial interests or personal relationships that could have appeared to influence the work reported in this paper.

Acknowledgements

This study was possible thanks to funding and support from the Shimizu Corporation, the Onassis Foundation and the National Research Fund of Luxembourg. The authors would also like to thank Paul Crudge and Alfredo Olivo for their assistance during the experiments.

Data availability

Data will be made available on request.

References

[1] L. Gardner, Metal additive manufacturing in structural engineering – review, advances, opportunities and outlook, Structures 47 (2023) 2178–2193.
[2] I.H. Shah, N. Hadjipantelis, L. Walter, R.J. Myers, L. Gardner, Environmental life cycle assessment of wire arc additively manufactured structural components, J. Clean. Prod. 389 (2023) 136071.
[3] X. Meng, L. Gardner, Hybrid construction featuring wire arc additive manufacturing: review, concepts, challenges and opportunities, Eng. Struct. 326 (2025) 119337.
[4] H. Pant, A. Arora, G.S. Gopakumar, U. Chadha, A. Saeidi, A.E. Patterson, Applications of wire arc additive manufacturing (WAAM) for aerospace component manufacturing, Int. J. Adv. Manuf. Technol. 127 (11–12) (2023) 4995–5011.
[5] A. Josten, M. Höfemann, Arc-welding based additive manufacturing for body reinforcement in automotive engineering, Weld. World 64 (8) (2020) 1449–1458.
[6] B. Weber, X. Meng, R. Zhang, M. Nitawaki, T. Sagawa, L. Gardner, Tensile behaviour of WAAM high strength steel material and members, Mater. Des. 237 (2024) 112517.
[7] B. Weber, X. Meng, L. Gardner, Local buckling behaviour of wire arc additively manufactured steel I-sections under axial compression and combined loading, Thin-Walled Struct. 211 (2025) 113027.
[8] V. Laghi, M. Palermo, L. Tonelli, G. Gasparini, V.A. Girelli, L. Ceschini, T. Trombetti, Mechanical response of dot-by-dot wire-and-arc additively manufactured 304L stainless steel bars under tensile loading, Constr. Build. Mater. 318 (2022) 125925.
[9] M.T. Chen, Y. Chen, W. Zuo, X. Yun, O. Zhao, S.W. Liu, et al., Experimental investigation on the tensile behavior of wire arc additively manufactured duplex stainless steel plates, Eng. Struct. 321 (2024) 118764.
[10] M.T. Chen, T. Zhang, Z. Gong, W. Zuo, Z. Wang, L. Zong, et al., Mechanical properties and microstructure characteristics of wire arc additively manufactured high-strength steels, Eng. Struct. 300 (2024) 117092.
[11] M.T. Chen, Y. Chen, C. Huang, L. Gardner, O. Zhao, Experimental investigation of fatigue crack growth in wire arc additively manufactured ER2209 duplex stainless steel, J. Constr. Steel Res. 231 (2025) 109615.
[12] C. Huang, L. Li, N. Pichler, E. Ghafoori, L. Susmel, L. Gardner, Fatigue testing and analysis of steel plates manufactured by wire-arc directed energy deposition, Addit. Manuf. 73 (2023) 103696.

[13] Y. Chen, M.T. Chen, O. Zhao, B. Rossi, X. Ruan, Fatigue crack growth behavior of wire arc additively manufactured 316L austenitic stainless steel, Thin-Walled Struct. 212 (2025) 113182.
[14] J. Lange, T. Feucht, M. Erven, 3D printing with steel: additive manufacturing for connections and structures, Steel Constr. 13 (3) (2020) 144–153.
[15] X. Guo, P. Kyvelou, J. Ye, L.H. Teh, L. Gardner, Experimental investigation of wire arc additively manufactured steel single-lap shear bolted connections, Thin-Walled Struct. 181 (2022) 110029.
[16] P. Kyvelou, A. Spinasa, L. Gardner, Testing and analysis of optimized wire arc additively manufactured steel trusses, J. Struct. Eng. 150 (3) (2024) 04024008.
[17] V. Laghi, M. Palermo, G. Gasparini, T. Trombetti, Computational design and manufacturing of a half-scaled 3D-printed stainless steel diagrid column, Addit. Manuf. 36 (2020) 101505.
[18] R.B. Cruise, L. Gardner, Residual stress analysis of structural stainless steel sections, J. Constr. Steel Res. 64 (3) (2008) 352–366.
[19] J. Wang, L. Gardner, Flexural buckling of hot-finished high strength steel SHS and RHS columns, J. Struct. Eng. ASCE 143 (6) (2017) 04017028.
[20] J.L. Ma, T.M. Chan, B. Young, Material properties and residual stresses of cold-formed high strength steel hollow sections, J. Constr. Steel Res. 109 (2015) 152–165.
[21] M. Theofanous, T.M. Chan, L. Gardner, Flexural behaviour of stainless steel oval hollow sections, Thin-Walled Struct. 47 (6–7) (2009) 776–787.
[22] A. Ermakova, J. Razavi, S. Cabeza, E. Gadalinska, M. Reid, A. Paradowska, S. Ganguly, F. Berto, A. Mehmanparast, The effect of surface treatment and orientation on fatigue crack growth rate and residual stress distribution of wire arc additively manufactured low carbon steel components, J. Mater. Res. Technol. 24 (2023) 2988–3004.
[23] J.R. Hönnige, P.A. Colegrove, S. Ganguly, E. Eimer, S. Kabra, S. Williams, Control of residual stress and distortion in aluminium wire + arc additive manufacture with rolling, Addit. Manuf. 22 (2018) 775–783.
[24] M. Kucukler, L. Gardner, L. Macorini, Lateral-torsional buckling assessment of steel beams through a stiffness reduction method, J. Constr. Steel Res. 109 (2015) 87–100.
[25] O. Zhao, L. Gardner, B. Young, Behaviour and design of stainless steel SHS and RHS beam-columns, Thin-Walled Struct. 106 (2016) 330–345.
[26] B. Ahmad, X. Zhang, H. Guo, M.E. Fitzpatrick, L.M.S.C. Neto, S. Williams, Influence of deposition strategies on residual stress in wire + arc additive manufactured titanium Ti-6Al-4V, Metals 12 (2) (2022) 253.
[27] W. Huang, Q. Wang, N. Ma, H. Kitano, Distribution characteristics of residual stresses in typical wall and pipe components built by wire arc additive manufacturing, J. Manuf. Process. 82 (2022) 434–447.
[28] P.J. Withers, M. Turski, L. Edwards, P.J. Bouchard, D.J. Buttle, Recent advances in residual stress measurement, Int. J. Press. Vessels Pip. 85 (3) (2008) 118–127.
[29] R. Li, J. Xiong, Y. Lei, Investigation on thermal stress evolution induced by wire and arc additive manufacturing for circular thin-walled parts, J. Manuf. Process. 40 (2019) 59–67.
[30] Y. Peng, J. Zhao, L. Chen, J. Dong, Residual stress measurement combining blind-hole drilling and digital image correlation approach, J. Constr. Steel Res. 176 (2021) 106346.
[31] H. Shen, J. Lin, Z. Zhou, B. Liu, Effect of induction heat treatment on residual stress distribution of components fabricated by wire arc additive manufacturing, J. Manuf. Process. 75 (2022) 331–345.
[32] P. Kyvelou, C. Huang, J. Li, L. Gardner, Residual stresses in steel I-sections strengthened by wire arc additive manufacturing, Structures 60 (2024) 105828.
[33] N. Tebedge, G. Alpsten, L. Tall, Residual-stress measurement by the sectioning method: a procedure for residual-stress measurements by the sectioning method is described. Two different hole-drilling methods were performed and the results are compared, Exp. Mech. 13 (2) (1973) 88–96.
[34] D. Boruah, N. Dewagtere, B. Ahmad, R. Nunes, J. Tacq, X. Zhang, H. Guo, W. Verlinde, W. De Waele, Digital image correlation for measuring full-field residual stresses in wire and arc additive manufactured components, Materials 16 (4) (2023) 1702.
[35] C. Liu, C. Lin, J. Wang, J. Wang, L. Yan, Y. Luo, M. Yang, Residual stress distributions in thick specimens excavated from a large circular wire+arc additive manufacturing mockup, J. Manuf. Process. 56 (2020) 474–481.
[36] Q. Yuan, C. Liu, W. Wang, M. Wang, Residual stress distribution in a large specimen fabricated by wire-arc additive manufacturing, Sci. Technol. Weld. Join. 28 (2) (2023) 137–144.
[37] F. Martina, M.J. Roy, B.A. Szost, S. Terzi, P.A. Colegrove, S.W. Williams, P. J. Withers, J. Meyer, M. Hofmann, Residual stress of as-deposited and rolled wire+arc additive manufacturing Ti–6Al–4V components, Mater. Sci. Technol. 32 (14) (2016) 1439–1448.
[38] P.A. Colegrove, H.E. Coules, J. Fairman, F. Martina, T. Kashoob, H. Mamash, L. D. Cozzolino, Microstructure and residual stress improvement in wire and arc additively manufactured parts through high-pressure rolling, J. Mater. Process. Technol. 213 (10) (2013) 1782–1791.
[39] B.A. Szost, S. Terzi, F. Martina, D. Boisselier, A. Prytuliak, T. Pirling, M. Hofmann, D.J. Jarvis, A comparative study of additive manufacturing techniques: residual stress and microstructural analysis of CLAD and WAAM printed Ti–6Al–4V components, Mater. Des. 89 (2016) 559–567.
[40] T. Klein, P. Spoerk-Erdely, C. Schneider-Broeskamp, J.P. Oliveira, G. Abreu Faria, Residual stresses in a wire and arc-directed energy-deposited Al–6Cu–Mn (ER2319) alloy determined by energy-dispersive high-energy X-ray diffraction, Metall. Mater. Trans. A 55 (3) (2024) 736–744.
[41] J. Zhang, X. Wang, S. Paddea, X. Zhang, Fatigue crack propagation behaviour in wire+arc additive manufactured Ti-6Al-4V: effects of microstructure and residual stress, Mater. Des. 90 (2016) 551–561.
[42] J. Sun, J. Hensel, M. Köhler, K. Dilger, Residual stress in wire and arc additively manufactured aluminum components, J. Manuf. Process. 65 (2021) 97–111.
[43] A. Nycz, Y. Lee, M. Noakes, D. Ankit, C. Masuo, S. Simunovic, J. Bunn, L. Love, V. Oancea, A. Payzant, C.M. Fancher, Effective residual stress prediction validated with neutron diffraction method for metal large-scale additive manufacturing, Mater. Des. 205 (2021) 109751.
[44] J. Xiong, Y. Lei, R. Li, Finite element analysis and experimental validation of thermal behavior for thin-walled parts in GMAW-based additive manufacturing with various substrate preheating temperatures, Appl. Therm. Eng. 126 (2017) 43–52.
[45] Q. Wu, T. Mukherjee, A. De, T. DebRoy, Residual stresses in wire-arc additive manufacturing – Hierarchy of influential variables, Addit. Manuf. 35 (2020) 101355.
[46] X. Lu, X. Lin, M. Chiumenti, M. Cervera, Y. Hu, X. Ji, L. Ma, H. Yanga, W. Huang, Residual stress and distortion of rectangular and S-shaped Ti-6Al-4V parts by Directed energy deposition: modelling and experimental calibration, Addit. Manuf. 26 (2019) 166–179.
[47] J. Gu, J. Ding, S.W. Williams, H. Gu, J. Bai, Y. Zhai, P. Ma, The strengthening effect of inter-layer cold working and post-deposition heat treatment on the additively manufactured Al–6.3Cu alloy, Mater. Sci. Eng. A 651 (2016) 18–26.
[48] J. Yang, P. Kyvelou, M.A. Wadee, L. Gardner, Simulation and prediction of residual stresses in WAAM-strengthened I-sections, Structures 69 (2024) 107248.
[49] Yang J., Wadee M.A., Gardner L. Residual stresses in steel I-section beams strengthened by wire arc additive manufacturing. *J. Constr. Steel Res.* (in press).
[50] M.D. Barath Kumar, M. Manikandan, Assessment of process, parameters, residual stress mitigation, post treatments and finite element analysis simulations of wire arc additive manufacturing technique, Met. Mater. Int. 28 (1) (2022) 54–111.
[51] A.A. Alrumayh, H.F. Nied, Simulation of residual stresses during the wire arc additive manufacturing (WAAM) process, Math. Model. Weld Phenom. 13 (2022) 283–303.
[52] J. Ding, P. Colegrove, J. Mehnen, S. Ganguly, P.M. Sequeira Almeida, F. Wang, S. Williams, Thermo-mechanical analysis of wire and arc additive layer manufacturing process on large multi-layer parts, Comput. Mater. Sci. 50 (12) (2011) 3315–3322.
[53] T.M. Chan, L. Gardner, K.H. Law, Structural design of elliptical hollow sections: a review, Proc. Inst. Civ. Eng. Struct. Build. 163 (6) (2010) 391–402.
[54] A.I. Osofero, M.A. Wadee, L. Gardner, Experimental study of critical and post-buckling behaviour of prestressed stayed columns, J. Constr. Steel Res. 79 (2012) 226–241.
[55] F. Wang, B. Young, L. Gardner, Experimental study of square and rectangular CFDST sections with stainless steel outer tubes under axial compression, J. Struct. Eng. 145 (11) (2019) 04019139.
[56] AWS A5.28/A5.28M:2005, Specification For Low-Alloy Steel Electrodes and Rods For Gas Shielded Arc Welding, American Welding Society, 2005.
[57] R. Ziemian, Guide to Stability Design Criteria For Metal Structures, John Wiley & Sons Inc, New Jersey, US, 2010.
[58] LaVision GmbH, DaVis 10, https://www.lavision.de/en/products/davis-software/, Version 595 10.2.1.
[59] Oqton, Inc, Geomagic Wrap. https://www.oqton.com/geomagic-wrap, 2017. Version 2017.0.2:64.
[60] A. Spinasa, B. Weber, X. Meng, R. Zhang, M. Nitawaki, L. Gardner, Influence of process parameters on the physical and material properties of WAAM steels, Constr. Build. Mater. 479 (2025) 141078.
[61] A. Stamenkovic, M. Gardner, Effect of residual stresses on the column behaviour of hot-finished steel structural hollow sections, Proc. Inst. Civ. Eng. 75 (4) (1983) 599–616.
[62] X. Meng, B. Weber, M. Nitawaki, L. Gardner, Optimisation and testing of wire arc additively manufactured steel stub columns, Thin-Walled Struct. 189 (2023) 110857.
[63] EN 1993-1-1:2022, Eurocode 3 - Design of Steel Structures - Part1-1: General rules and Rules For Buildings, European Committee for Standardization, 2022.
[64] H.X. Yuan, Y.Q. Wang, L. Gardner, Y.J. Shi, Local–overall interactive buckling of welded stainless steel box section compression members, Eng. Struct. 67 (2014) 62–76.
[65] O. Zhao, B. Rossi, L. Gardner, B. Young, Experimental and numerical studies of ferritic stainless steel cross-sections under combined compression and bending, J. Struct. Eng. 142 (2) (2016) 04015110.
[66] D. Fan, M. Gao, C. Li, J. Huang, X. Yu, Residual stress and microstructure properties by trailing cooling of argon gas of wire and arc additive manufacturing, J. Manuf. Process. 77 (2022) 32–39.
[67] X. Meng, A. Pullen, X. Guo, X. Yun, L. Gardner, 3D laser scanning and DIC in structural testing: state-of-the-art, best practice and effective use, Eng. Struct. 345 (2025) 121055.